Microstructural Stability and Evolution in a New Polycrystalline Ni-Base Superalloy

G.J. WISE, N.L. CHURCH, C.E.P. TALBOT, P.M. MIGNANELLI, M.C. HARDY, N.G. JONES, and H.J. STONE

Polycrystalline Ni-base superalloys that offer equivalent or superior performance to current commercial alloys at lower overall cost are of widespread industrial interest. In this work, a new polycrystalline Ni-base superalloy with low elemental cost has been characterized and compared to current commercially available alternatives. Through a combination of scanning electron microscopy, thermal analysis, synchrotron X-ray diffraction, and hardness testing, a broad preliminary investigation of fundamental alloy properties has been performed, identifying the key areas for further alloy development opportunities.

I. INTRODUCTION

THE increasing service requirements for polycrystalline Ni-base superalloys used in civil aviation and power generation applications have continued to motivate the development of new alloys.[1,2] Much of this activity has focussed on increasing the volume fraction of strengthening precipitates, primarily by increasing the content of the precipitate forming elements Al and Ti.[3–6] In addition, solid solution strengthening has been enhanced by increasing the content of refractory metals. While these strengthening methods are effective, the alloying additions increase the raw elemental cost of the alloy, the alloy density, and sensitivity to solidification anomalies, including freckle and dirty white-spot.[7–11] In addition, the lower workability, increased risk of cracking, and difficulties in achieving uniform recrystallization of such alloys[12–16] necessitate multiple processing steps or the use of powder metallurgy (PM) routes, which further increase material costs.

For components that do not operate in such demanding conditions, the properties offered by powder-processed alloys are not generally required, and lower-cost, cast and wrought (C&W) alloys are more attractive. For these applications, the most widely used Ni-base superalloy has historically been Inconel718® (IN718). This alloy is strengthened by a dispersion of γ'' superlattice precipitates (Ni$_3$Nb, D0$_{22}$, tetragonal, $I4/mmm$),[17] rather than the γ' (Ni$_3$Al, L1$_2$, cubic, $Pm\overline{3}m$) superlattice precipitates typically encountered in many other Ni-base superalloys.[18,19] Notably, γ'' precipitation in IN718 is relatively slow compared to γ' precipitation in other superalloys, with TTT diagrams indicating the onset of precipitation after approximately 10 hours at 680 °C.[20] The slow kinetics ensure the alloy has good processability, as deformation processing and machining operations can be performed in the solution-treated condition, with aging of the final component to provide the required mechanical properties. Exhibiting a low propensity for solidification defects during melt and remelt stages, combined with a high Fe content, the alloy demonstrates low elemental cost and is also readily joinable due to a low susceptibility to strain-age cracking.[21,22] This balance of properties has resulted in widespread industrial uptake, where it outperforms Waspaloy for service applications below 650 °C.[23–26] It has been estimated that the manufacture of IN718 accounts for over 35 pct of all wrought superalloy production.[27] Nevertheless, IN718 is limited to applications below 650 °C due to coarsening and eventual dissolution of the strengthening precipitates above this temperature. These processes are associated with a concomitant loss of tensile and creep performance. For significant durations at elevated temperatures, the metastable γ'' ultimately transforms to the stable δ phase (Ni$_3$Nb, D0$_a$, orthorhombic, $Pmmn$), which is also considered deleterious to the mechanical behavior.[28,29]

Due to the higher temperatures and loads that will be encountered in the next generation of engine designs, alloys with higher temperature capability than IN718 are required. Alloys that improve on the properties of IN718, while still offering considerable cost savings over

G.J. WISE, N.L. CHURCH, C.E.P. TALBOT, N.G. JONES, and H.J. STONE are with the Department of Materials Science and Metallurgy, University of Cambridge, 27 Charles Babbage Road, Cambridge CB3 0FS, UK. Contact e-mail: hjs1002@cam.ac.uk P.M. MIGNANELLI and M.C. HARDY are with Rolls-Royce plc., PO BOX 31, Derby DE24 8BJ, UK.

the highly alloyed, powder-processed alloys used for the most demanding applications, are therefore of significant industrial value. One alloy of this type that has superseded IN718 in some applications is ATI 718Plus® (718Plus), designed with a higher Al and Ti content to favor the precipitation of γ' over γ'', alongside other compositional modifications to improve solid solution strengthening and creep performance.[30,31] This alloy offers an increased operating temperature limit of around 55 °C compared to IN718, with only a minor increase in cost.

There is a significant research effort to explore the cost-performance design space between existing cast and wrought alloys such as 718Plus and powder-processed material such as René88DT and RR1000.[16] One approach has been to make compositional modifications to highly alloyed commercial materials to produce derivatives that are more amenable to manufacture *via* cast and wrought processes. Examples include Alloy 720Li (720Li)[32] and more recently René65.[33,34] While both of these advanced cast and wrought alloys improve on the properties of 718Plus, 720Li requires optimized homogenization of the as-cast ingot and is known to possess a narrow processing window for forging operations.[13,14,35,36] Being one of the most highly alloyed materials that can still be processed by the cast and wrought route, 720Li is typically considered to be the alloying limit beyond which processing by powder metallurgy is required.[36] René65 also demonstrates issues with workability, with large unrecrystallized grains persisting after ingot to billet conversion.[37–39] Similar effects have been reported during the cogging process for the newly developed AD730™,[40,41] which offers some improved mechanical performance, greater workability, and lower costs compared to 720Li, but still requires multiple deformation steps to recrystallize the ingot to billet.[42–44]

A common feature of these advanced cast and wrought alloys is their relatively high γ' volume fraction between 35 and 40 pct. This is a result of the high content of precipitate forming elements (Al and Ti) compared to IN718. While this provides improved mechanical properties, it is indicative that these new alloys occupy the high-performance region of the design space between cast & wrought material and powder-processed alloys. The high Al and Ti contents, combined with elevated levels of Mo and W, also result in an increased propensity to freckle defects during remelting.[8,9] When combined with the extensive deformation processing that they require to produce billet, these alloys are not generally considered to be low cost. It is contended that further exploration of the cost-performance design space may yield new alloys better suited for applications in the intermediate stress and temperature regime.

More recently, efforts to develop lower-cost alloys have led to the production of VDM780P,[45] which was designed to offer similar mechanical properties to IN718, but with a wider forging window, enhanced microstructural stability, and a proposed application temperature of 750 °C. Uniform recrystallized microstructures can be obtained in forged product,

although the kinetics are relatively slow, requiring a 5-minute hold at 1050 °C post-deformation, which gives a grain size on the order of 25 μm.[46] Additionally, the high Co content of this alloy (24.5 at. pct) introduces greater fluctuations in the raw elemental cost compared to alloys such as IN718 and 718Plus.

In this work, the microstructure, phase equilibria, thermal stability, and aging response of a new polycrystalline Ni-base superalloy have been assessed. The new alloy has been designed to improve on the mechanical properties and thermal stability of IN718, with a proposed operating temperature of 725 °C. It has also been designed to have lower elemental and processing costs compared to 720Li, with a reduced γ' volume fraction as a result of a lower Al and Ti content. This is expected to reduce the susceptibility to solidification defects and facilitate easier ingot to billet conversion with fully recrystallized microstructures.

While the new alloy is ultimately intended to be processed *via* cast and wrought methods, in this preliminary study, a powder metallurgy route was used to produce the alloy. This was chosen so that the effects of composition and microstructure could be investigated, without the significant investment required to optimize the alloy for ingot metallurgy. Typically, this optimization process comprises the evaluation and specification of appropriate primary melting, secondary remelting, and ingot conversion practices, combined with minor compositional modifications of the interstitial and grain boundary-strengthening elements C, B, and Zr. Nevertheless, it is recognized that a powder-processed version of the alloy is likely to produce optimized properties, with reduced levels of microsegregation and the elimination of macrosegregation-related solidification anomalies leading to greater microstructural homogeneity. In addition, powder-processed material can also exhibit a finer grain size than C&W product, with superior mechanical strength and fatigue resistance. Importantly, the choice of powder processing is not expected to adversely affect the phase stability, precipitation kinetics, or microstructural evolution that takes place in the alloy, features that must be characterized and understood as part of any new alloy development program. Such an understanding is crucial in evaluating whether further development work is warranted, and, if so, what trials need to be performed. Using a combination of scanning electron microscopy, electron back-scattered diffraction, thermal analysis, dilatometry, and synchrotron X-ray diffraction, the new alloy has been characterized and compared to current commercially available materials.

II. EXPERIMENTAL METHODS

The nominal composition of the alloy studied in this research (Alloy 1) is provided in Table I and is covered by United States Patent US10287654.[47] For comparative purposes, the compositions of several other commercial polycrystalline Ni-base superalloys in both atomic and weight percent are also included.[3,6,30,32,33,40,45] A compact of the alloy was

Table I. Nominal Composition of the Alloy Studied in This Research (Alloy 1) and Other Selected Commercial Polycrystalline Ni-Base Superalloys in at. pct (wt pct)

at. pct (wt pct)	Ni	Cr	Co	Fe	Al	Nb	Mo	W	Ta	Ti	Hf	C	B	Zr
Alloy 1	bal.	20.0 (18.0)	8.15 (8.30)	7.85 (7.60)	4.65 (2.17)	3.55 (5.71)	2.50 (4.15)	—	—	0.12 (0.10)	—	0.07 (0.015)	0.08 (0.015)	0.025 (0.039)
Reference Compositions of Selected Cast and Wrought Polycrystalline Ni-Base Superalloys														
IN718[30]	bal.	21.1 (19.0)	—	19.2 (18.5)	1.29 (0.60)	3.21 (5.15)	1.81 (3.00)	—	—	1.09 (0.90)	—	0.19 (0.040)	0.02 (0.003)	—
718Plus[30]	bal.	20.1 (18.0)	8.97 (9.10)	9.88 (9.50)	3.12 (1.45)	3.38 (5.40)	1.64 (2.70)	0.32 (1.00)	—	0.91 (0.75)	—	0.10 (0.020)	0.03 (0.005)	—
AD730[40]	bal.	17.3 (15.7)	8.28 (8.50)	4.11 (4.00)	4.79 (2.25)	0.68 (1.10)	1.85 (3.10)	0.84 (2.70)	—	4.08 (3.40)	—	0.07 (0.015)	0.05 (0.010)	0.019 (0.030)
VDM780[48]	bal.	20.0 (18.0)	24.5 (25.0)	0.60 (0.58)	4.30 (2.01)	3.40 (5.47)	1.80 (3.00)	—	—	0.4 (0.33)	—	*	*	—
René65[33]	bal.	17.9 (16.0)	12.8 (13.0)	1.04 (1.00)	4.53 (2.10)	0.44 (0.70)	2.43 (4.00)	1.27 (4.00)	—	4.50 (3.70)	—	—	0.09 (0.016)	0.03 (0.050)
720Li[32]	bal.	17.3 (16.0)	14.1 (14.7)	—	5.22 (2.50)	—	1.76 (3.00)	0.38 (1.25)	—	5.89 (5.00)	—	0.05 (0.010)	0.08 (0.015)	0.02 (0.030)
Reference Compositions of Selected Powder Metallurgy Polycrystalline Ni-Base Superalloys														
RR1000[3]	bal.	16.5 (15.0)	17.9 (18.5)	—	6.35 (3.00)	—	2.98 (5.00)	—	0.63 (2.00)	4.30 (3.60)	0.16 (0.50)	0.14 (0.030)	0.11 (0.020)	0.04 (0.060)
René88DT[6]	bal.	17.9 (16.0)	12.8 (13.0)	—	4.53 (2.10)	0.44 (0.70)	2.43 (4.00)	1.27 (4.00)	—	4.50 (3.70)	—	0.15 (0.030)	0.08 (0.015)	0.02 (0.030)

The alloy composition studied in this research is covered by US Patent US10287654.
*The C and B contents in VDM780 are similar to IN718.

produced *via* a powder metallurgy route by ATI Specialty Materials, Pittsburgh. This comprised vacuum induction melting, gas atomization to form a powder, screening to −270 mesh (53 μm), and filling into a mild steel container. This was degassed and sealed before being hot isostatically pressed (HIP) at 100 MPa for 4 hours at 1050 °C. Compositional analysis was performed using Inductively Coupled Plasma-Optical Emission Spectroscopy (ICP-OES) and Combustion Infrared Absorption (for carbon) at ATI Specialty Materials in accordance with ASTM E2594 and E1019.

Slices of the As-HIP compact measuring 20 mm thick were taken for microstructural examination. Each slice was mounted in phenolic resin, followed by grinding using successively finer SiC abrasive papers to a 5 μm finish. Final polishing was performed using colloidal silica (OPS) to a 0.04 μm finish. Etching was conducted electrolytically, using a 10 pct by volume aqueous orthophosphoric acid (H_3PO_4) solution and an applied voltage between 3 and 5 V, for approximately 1 to 2 seconds.

Disk-shaped samples for differential scanning calorimetry (DSC) measuring 5 mm in diameter by 1 mm thick were produced by electro-discharge machining (EDM). DSC thermograms were obtained using a Netzsch 404 *F1 Pegasus®* DSC between 50 °C and 1450 °C, with a 10 °C min^{-1} heating and cooling rate, under flowing argon at 50 mL min^{-1}.

Scanning electron microscopy (SEM) was performed using a Zeiss GeminiSEM 300, operated at 15 kV using a 30 μm aperture. The imaging of the precipitate distributions after thermal exposure was acquired with a low accelerating voltage (3 kV) and an InLens SE detector. Elemental concentration maps were acquired *via* energy-dispersive X-ray spectroscopy (EDX), performed using an Oxford Instruments X-Flash^N 50 EDX spectrometer fitted to the same instrument. To optimize the EDX signal, an accelerating voltage of 25 kV, an aperture of 120 μm, and a working distance of 8.5 mm were used. EDX data were processed using the Oxford Instruments AZtec software package. Electron backscatter diffraction (EBSD) was performed using an Oxford Instruments SYMMETRY detector, an accelerating voltage of 25 kV, aperture size of 120 μm, a step size of 0.2 μm, and a dwell time of 2 ms. Processing of the EBSD data was conducted using the Oxford Instruments HKL CHANNEL5 software, with inverse pole figure (IPF) maps generated using the Tango package.

Synchrotron X-ray diffraction (sXRD) measurements were performed under experiment numbers MG30411 and MG31965 on the Joint Engineering and Environmental Processing beamline (I12-JEEP) at Diamond Light Source, Didcot, UK.[49] Samples were illuminated using a 0.5 × 0.5 mm^2 monochromatic beam, with wavelengths of 0.1557 Å and 0.1543 Å, corresponding to beam energies of 79.69 and 80.35 keV, respectively. Two-dimensional patterns were acquired using a transmission Debye–Scherrer geometry on a Pilatus 2M CdTe 2D area detector, with an exposure time of 1 s per

Table II. Composition of the γ′ Etchant (Precursor and Final), as Originally Defined in Ref. [54]

Part I	Part II
150 mL H_2O	15 mL HNO_3
150 mL HCl	25 mL H_2O
2.5 g MoO_3	30 mL part I

frame.[50] The sample-to-detector distance was approximately 833 mm, calibrated using CeO_2 (NIST standard) at multiple sample-to-detector distances.[51] One-dimensional diffraction patterns were obtained *via* full-range azimuthal integration of the 2D detector images using the DAWN software.[52,53] Phase identification was performed by comparing the diffraction patterns with reference patterns generated from structures obtained using the Inorganic Crystal Structure Database (ICSD © FIZ Karlsruhe GmbH).

Cylindrical samples for heat treatment and aging studies measuring 4 mm diameter × 10 mm long were extracted from the As-HIP compact slices using electro-discharge machining (EDM) and ground using SiC papers to a 15 μm finish. The samples were solution treated under vacuum for 1 hour at 1030 °C using a TA Instruments DIL805 dilatometer operated in quenching mode, using fused silica pushrods. Heating was performed inductively, with a linear heating rate of 10 °C s^{-1}, and cooling from the solution heat treatment temperature at a linear rate of 3 °C s^{-1}. Temperature control was achieved through the use of an S-type thermocouple spot-welded directly to the surface of each sample.

Subsequent heat treatments were performed in a laboratory box furnace at temperatures of 750 °C, 800 °C, 850 °C, and 900 °C, calibrated to ± 1 °C using an N-type thermocouple. Heat treatments were performed for the durations of 1, 2, 4, 10, 100, and 1000 hours. The heat-treated samples were prepared for examination using the same metallographic preparation route outlined earlier. Etching was performed using a γ′ etchant first described by Preuss *et al.*,[54] which is produced from a precursor with the compositions of both the precursor (Part I) and final etchant (Part II) given in Table II.

Scanning electron micrographs of the heat-treated samples were analyzed using ImageJ, with the resulting precipitate distributions (in equivalent circular diameter) statistically binned following the method described by Freedman and Diaconis.[55] The resulting histograms were subsequently fitted to a log-normal distribution using the IGOR Pro 8 software package in order to obtain the average precipitate diameter.

Vickers hardness measurements were obtained using a Qness Q30 A+ automatic hardness tester, operated with a 10-kg load. The values are given as the average of five indentations, along with the standard deviation of the measurements.

Table III. ICP-OES Measured Compositions of the Powder-Processed Material in at. pct (wt pct)

	Ni	Cr	Co	Fe	Al	Nb	Mo	Ti	C	B	Zr
Alloy 1	Bal.	20.0 (18.0)	8.14 (8.30)	7.96 (7.70)	4.56 (2.13)	3.47 (5.58)	2.58 (4.29)	0.15 (0.12)	0.07 (0.015)	0.09 (0.017)	0.02 (0.038)

III. RESULTS

A. Compositional Analysis

The experimentally determined compositions as measured by ICP-OES are given in Table III. The measured composition was within 0.2 wt pct of the nominal composition and was deemed sufficiently close to be suitable for the purposes of this study. Errors in the measurements are on the order of 0.01 pct.

B. Thermal Analysis

To identify appropriate solution heat treatment conditions, DSC was used to assess the solvus temperature of the strengthening precipitates. A DSC thermogram was obtained for the alloy in the As-HIP condition, with thermal events corresponding to phase transformations marked in Figure 1. Based on the work by Sponseller,[56] the sharp peak at 955 °C is characteristic of the dissolution of γ', with the maximum rate of dissolution (955 °C), the point of inflection (973 °C), and completion of dissolution (985 °C) represented with round markers. The event at 1183 °C is also observed in other superalloys and is attributable to the onset of liquation of any carbide species present in the material. Based on these findings, a nominal solution heat treatment temperature of 1030 °C was selected. This temperature was chosen to ensure precipitate dissolution, while minimizing grain growth and avoiding any incipient melting events.

C. Microstructure (As-HIP)

Scanning electron micrographs obtained for the alloy in the As-HIP condition as well as after solution heat treatment (SHT) are presented in Figure 2. The solution heat treatment at 1030 °C for 1 hour was performed under vacuum in a dilatometer, so that the post-SHT cooling rate (3 °C s^{-1}) could be precisely controlled and monitored. This allowed the production of further specimens for aging trials with a uniform and consistent distribution of precipitates. The micrographs in Figure 2 were taken across three length scales to highlight the microstructural features detected. In both the As-HIP and SHT conditions, a distribution of equiaxed grains was observed at low magnifications, some showing prominent annealing twins. At higher magnifications, a blocky precipitate phase was observed to decorate the prior particle boundaries (PPBs), while in the highest magnification image, pseudo-cuboidal precipitates were observed within the grains with a length scale on the order of 20 nm. After solution heat treatment, the
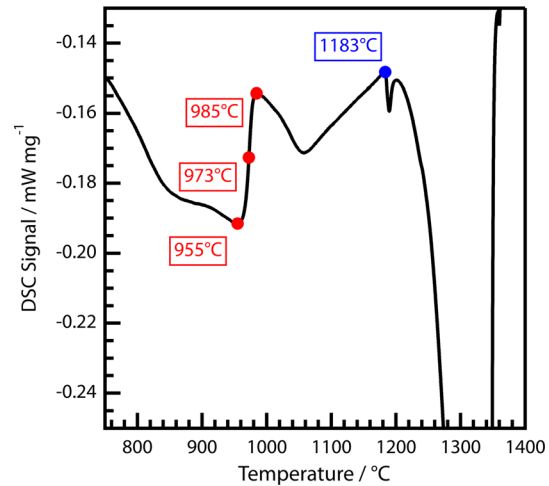

Fig. 1—DSC thermogram for the alloy in the As-HIP condition. The temperatures at which onset, inflection, and return to baseline were observed are marked in red. The temperature at which liquation of carbides occurred is marked in blue (Color figure online).

precipitates were observed to be considerably smaller, consistent with dissolution and reprecipitation.

The grain size distribution was investigated using EBSD in both the As-HIP and SHT conditions. Corner and edge grains were excluded from the analyses, as were changes in orientation due to {111} type twins. The grain size data were then statistically binned and fitted to a log-normal distribution using Igor Pro. The band contrast, IPF-Z maps, and associated histograms obtained from these data are shown in Figure 3. In both of the conditions investigated, no pronounced texture was observed. Also, in the solution heat-treated sample, no significant grain growth was exhibited when compared to the As-HIP condition.

D. Minority Phase ID

Further investigation of the phases decorating the prior particle boundaries was performed via elemental mapping and synchrotron X-ray diffraction. A back-scattered electron image and associated elemental concentration maps for the alloy are shown in Figure 4. Two distinct phases may be identified, a bright contrast (BC) phase with elevated Nb, Mo, and Zr and depleted Ni, Co, Cr, and Fe, and an intermediate contrast (IC) phase with similar elemental partitioning but exhibiting lower Nb and Zr levels, marked with red circles in Figure 4. The identities of these phases were determined from synchrotron diffraction data presented in Figure 5.
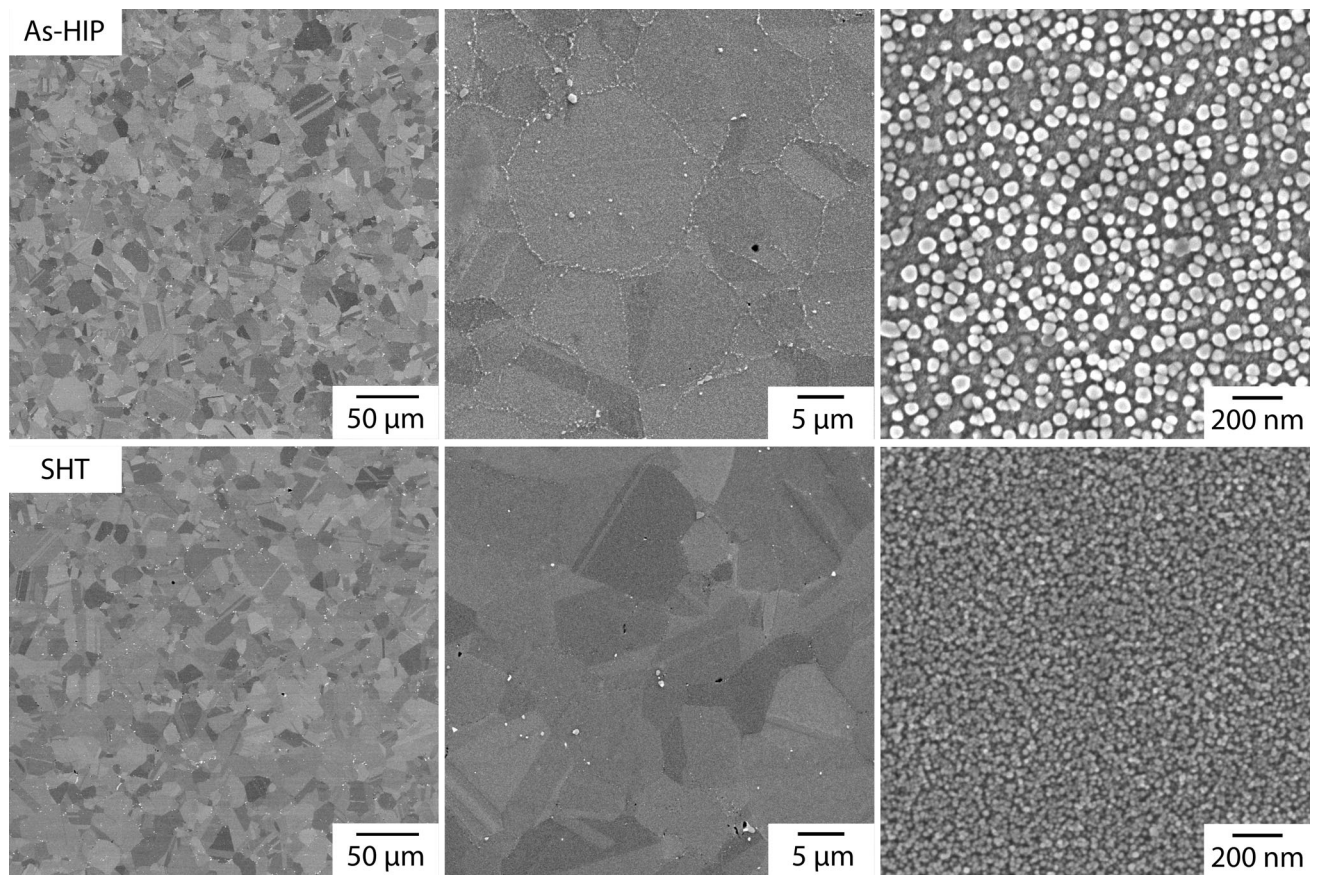
Fig. 2—Microstructural morphologies of the alloy in the As-HIP (top) and SHT (bottom) conditions across three different length scales.

The room-temperature diffraction pattern obtained for the alloy exhibited fundamental reflections corresponding to the γ matrix and γ' precipitates. Also visible were superlattice reflections for the γ', alongside the additional peaks attributable to MC and $M_{23}C_6$ carbides. These carbides are known to form in similar polycrystalline Ni-base superalloys.[57–59] These phases are also consistent with the features observed in Figure 4, with the bright contrast phase corresponding to the MC carbides, as a result of the higher Nb and Zr contents, and the intermediate contrast phase to the $M_{23}C_6$ carbides.

E. Precipitate Evolution and Long-Term Microstructural Stability

To assess the growth kinetics of the γ' precipitates, a series of heat treatments between 750 °C and 900 °C were performed for durations between 1 and 1000 hours. To ensure consistency of the initial microstructural condition, the samples were solution heat treated in a dilatometer at 1030 °C for 1 hour under vacuum and cooled at 3 °C s^{-1} to room temperature. This careful control of heat treatment conditions avoided the variability in starting γ' size that can often arise with air cooling. The SHT microstructure was shown earlier in the bottom row of Figure 2, exhibiting an ultrafine dispersion of precipitates. Because of this, a γ' etchant was used for the size measurements to avoid characterizing any subsurface precipitates. The precipitate morphologies after subsequent thermal exposure are shown in Figure 6, where dispersions of rounded precipitates that increased in diameter with both aging temperature and exposure duration were observed. (Note the change in scale for the 100 and 1000 hour exposures).

Low magnification images of the microstructure of the samples following thermal exposure for 100 hours or 1000 hours at temperatures between 750 °C and 900 °C are shown in Figure 7. No significant grain boundary precipitation was observed after exposure at 750 °C and 800 °C for 100 hours, with limited grain boundary precipitation visible in the sample exposed at 850 °C for 100 hours. This precipitation became more extensive after 100 hours at 900 °C. In the samples exposed for 1000 hours, the grain boundary precipitation was more extensive still, with fine precipitates decorating the grain boundaries at 750 °C. These precipitates became larger, more discrete, and facetted at the higher exposure temperatures. For exposure durations below 100 hours, no grain boundary precipitation (other than that detected in the SHT condition) was observed across all the temperatures studied.

These microstructural changes are likely to have a pronounced influence on the mechanical properties of the alloy. Therefore, it is important to characterize the
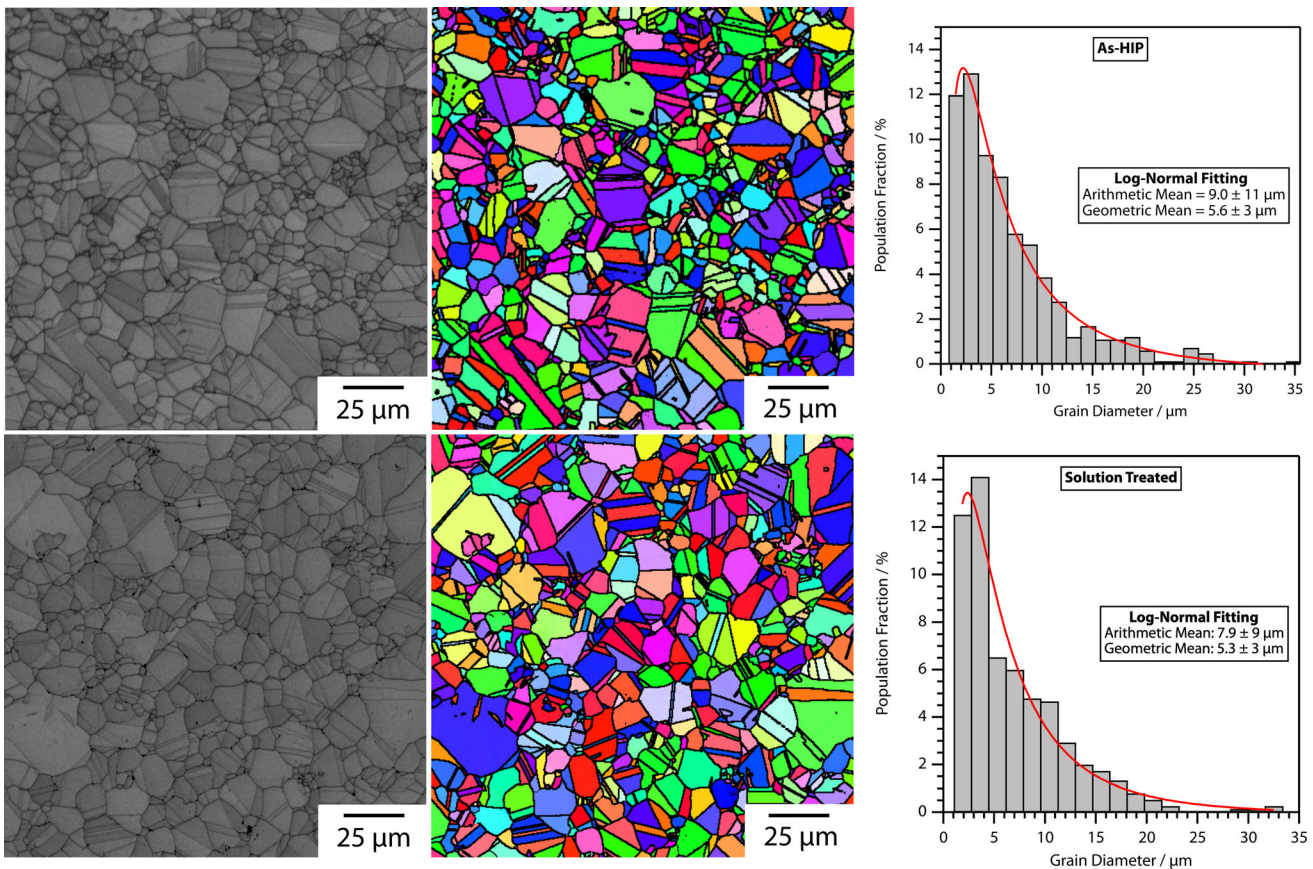
Fig. 3—Band contrast images (left), IPF-Z maps (center), and grain size histograms (right) obtained from the alloy in the As-HIP (top) and SHT condition (bottom).

phase formation, and the temperature regime over which it occurs. To further investigate the observed precipitation after long-term thermal exposure, additional exposures were performed on material in the SHT condition at 920 °C and 940 °C for 100 hours (below the experimentally determined γ' solvus of 955 °C). SEM micrographs are presented in Figure 8, where at 900 °C, needles of an acicular phase can be seen decorating some of the grain boundaries. The apparent volume fraction of these precipitates reduced after exposure at 920 °C, and they were not detected after exposure at 940 °C. The apparent dissolution of these precipitates suggests that the solvus temperature for their formation lies between 920 °C and 940 °C.

Synchrotron X-ray diffraction was used to investigate the identity of the phases formed in samples exposed for 100 and 1000 hours between 750 °C and 900 °C. The associated diffraction patterns are presented in Figure 9. In addition to the phases identified in the SHT condition, isolated peaks consistent with the δ phase were observed in all samples. These peaks were most apparent between 4.4 and 4.6 deg 2θ, as well as at 6.8 and 7.4 deg 2θ. The intensity of the peaks increased with aging time, indicative of a greater volume fraction of δ phase present in the microstructure and consistent with the qualitative microstructural observations from Figure 7.

Vickers hardness data were collected for all the conditions studied and are presented in Figure 10, with error bars representing one standard deviation. For reference, the hardness of the alloy in the SHT condition (1030 °C—1 hr followed by 3 °C s^{-1} cooling) was 388 ± 2 HV10, and is indicated by the dashed line in the figure. For the thermal exposures at 750 °C, 800 °C, and 850 °C, the hardness was initially greater than the SHT condition and the samples exposed at 750 °C and 800 °C demonstrated a hardening response with exposure time, increasing up to 450 HV10 after 100 hours at 750 °C and up to 430 HV10 after 4 hours at 800 °C. These peaks in hardness were followed by a slight decrease for longer exposures, yet still remained higher than the SHT condition. The 850 °C samples exhibited decreasing hardness with increasing exposure time, falling below that of the SHT condition after approximately 40 hours. In contrast, the samples exposed at 900 °C exhibited a lower hardness than the SHT condition even after only 1 hour of thermal exposure.

IV. DISCUSSION

A. Microstructure

The microstructural and diffraction analyses indicated that the alloy was solely γ' forming, with no evidence of any γ'' formation. This was expected given the relatively high Al:Nb ratio and is consistent with other alloys of
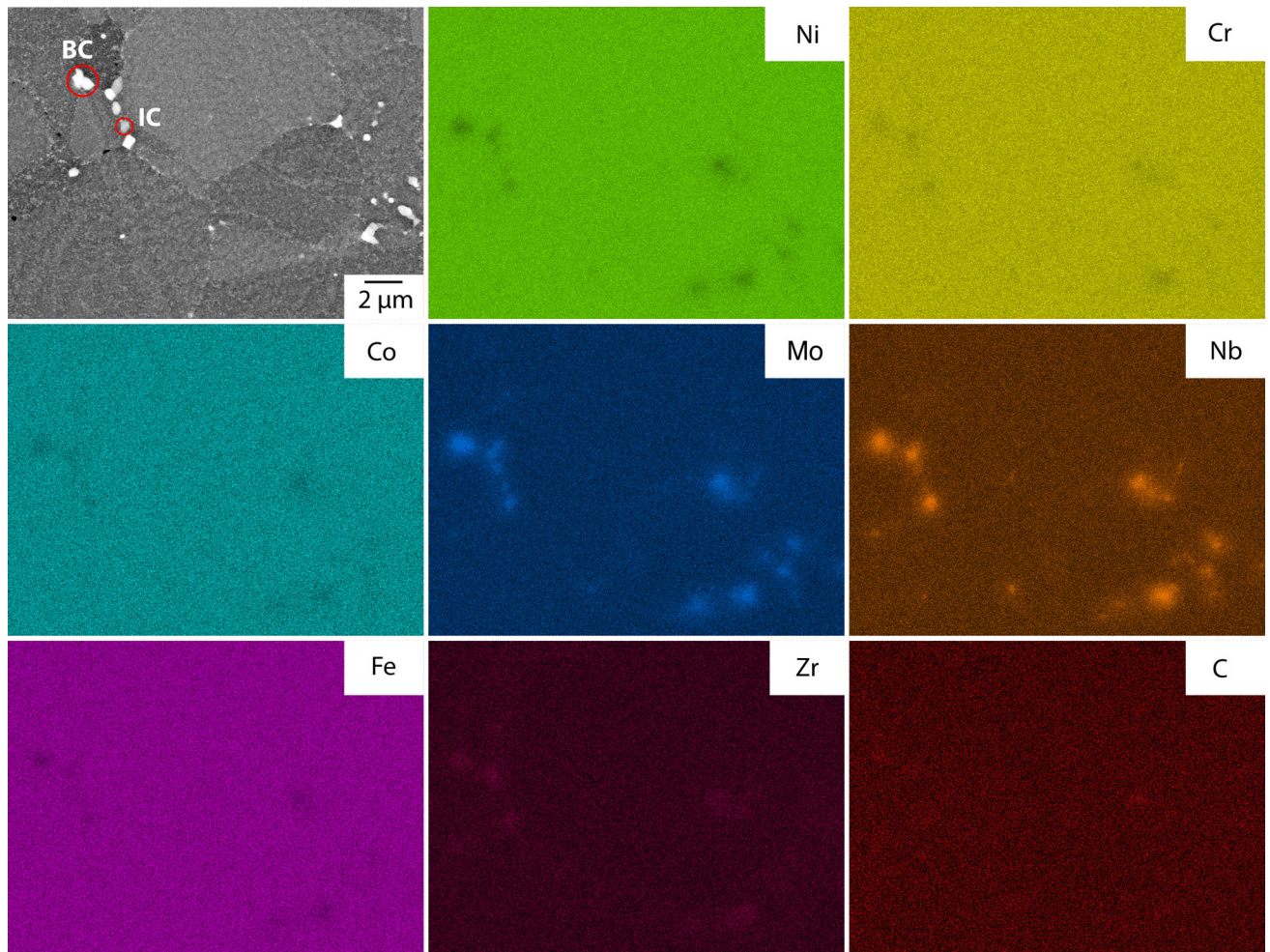
Fig. 4—Back-scattered electron image (top left) and corresponding EDX elemental concentration maps (individually labeled) highlighting the boundary phases present in the As-HIP condition.
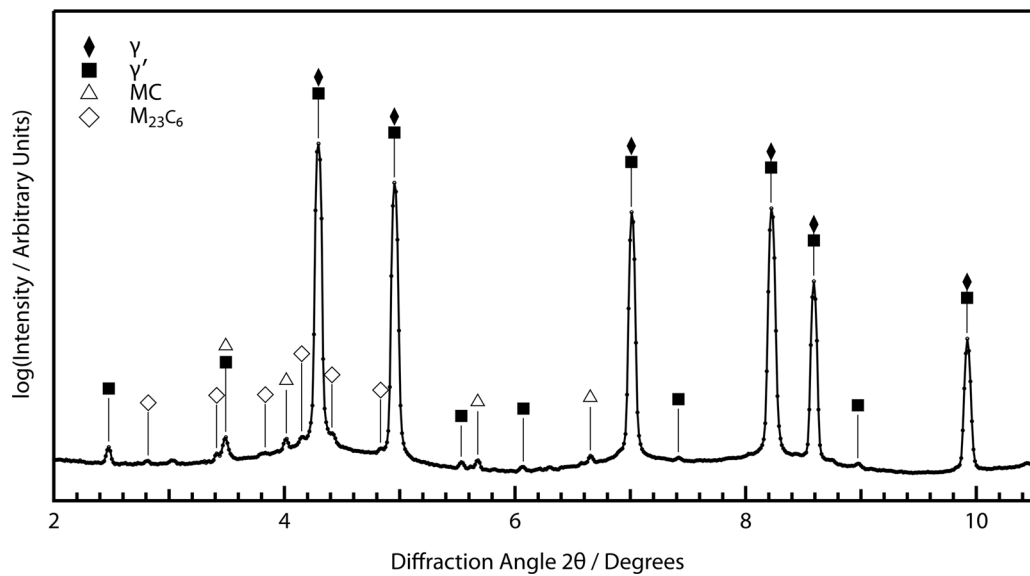

Fig. 5—Synchrotron X-ray diffraction pattern for the alloy at room temperature. Reflections corresponding to the γ, γ', MC, and $M_{23}C_6$ phases are indicated with markers.
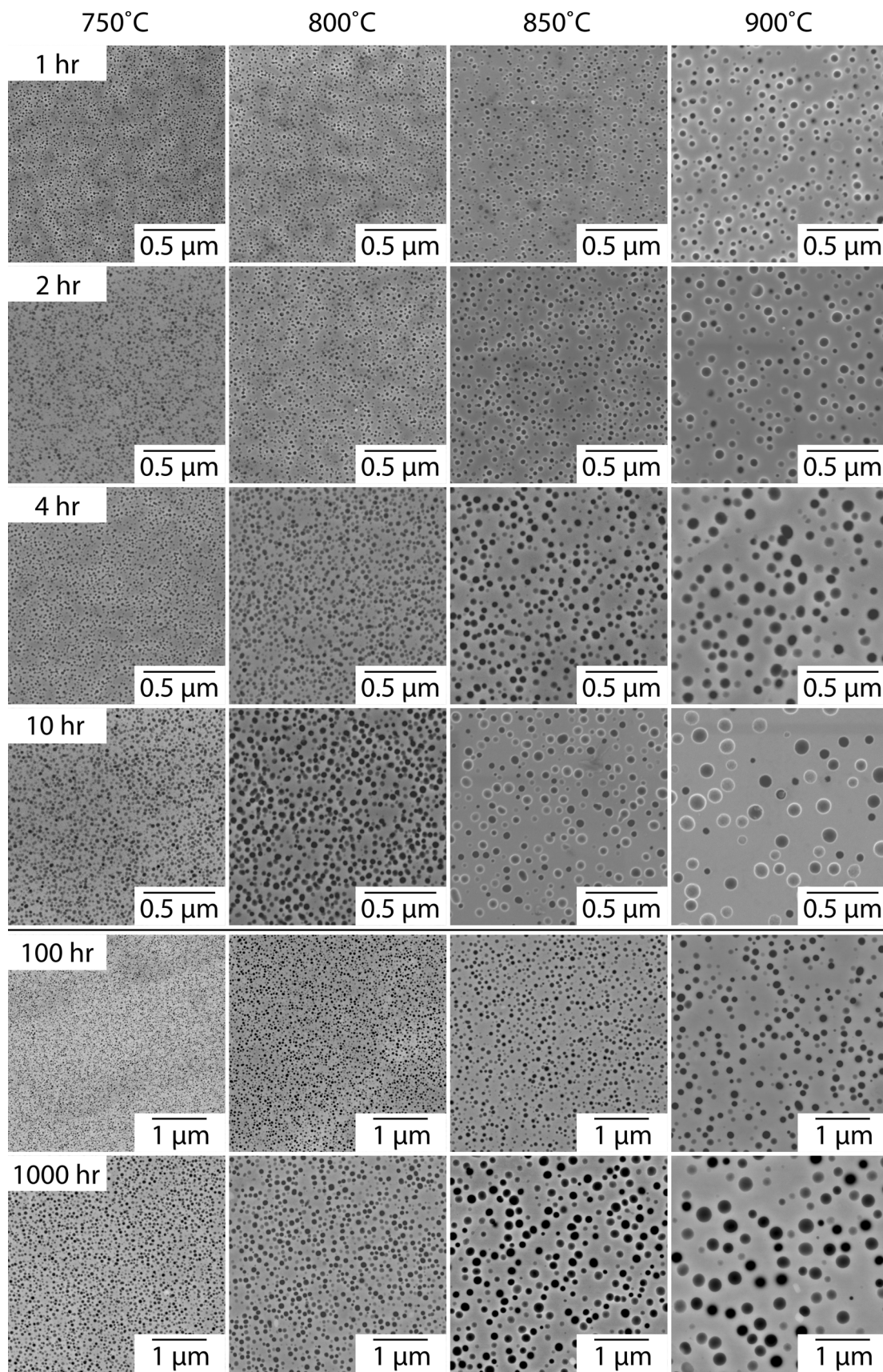
Fig. 6—Secondary electron SEM images showing the evolution of the precipitates as a function of time at temperatures between 750 °C and 900 °C for exposure durations 1-1000 hours. Note the change in scale bar for the 100 and 1000 hour exposures.
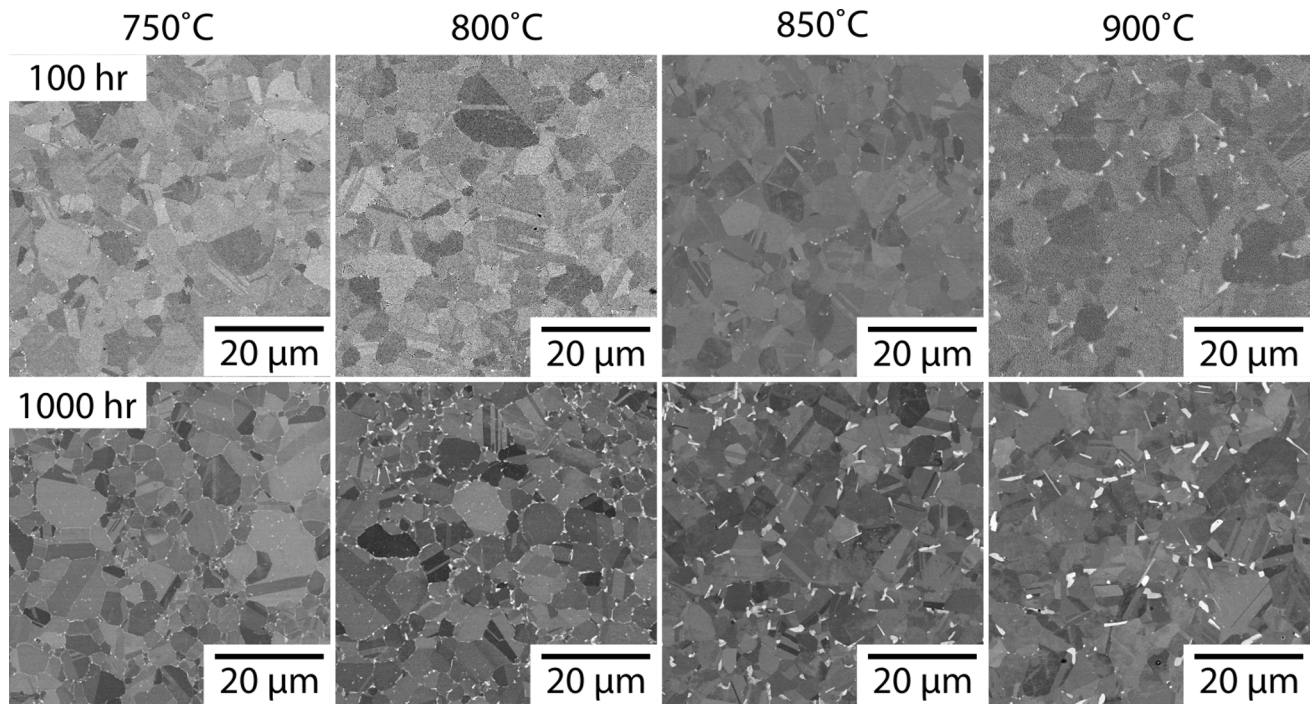
Fig. 7—SEM images showing the bulk precipitation observed after exposures for 100 and 1000 hours between 750 °C and 900 °C.
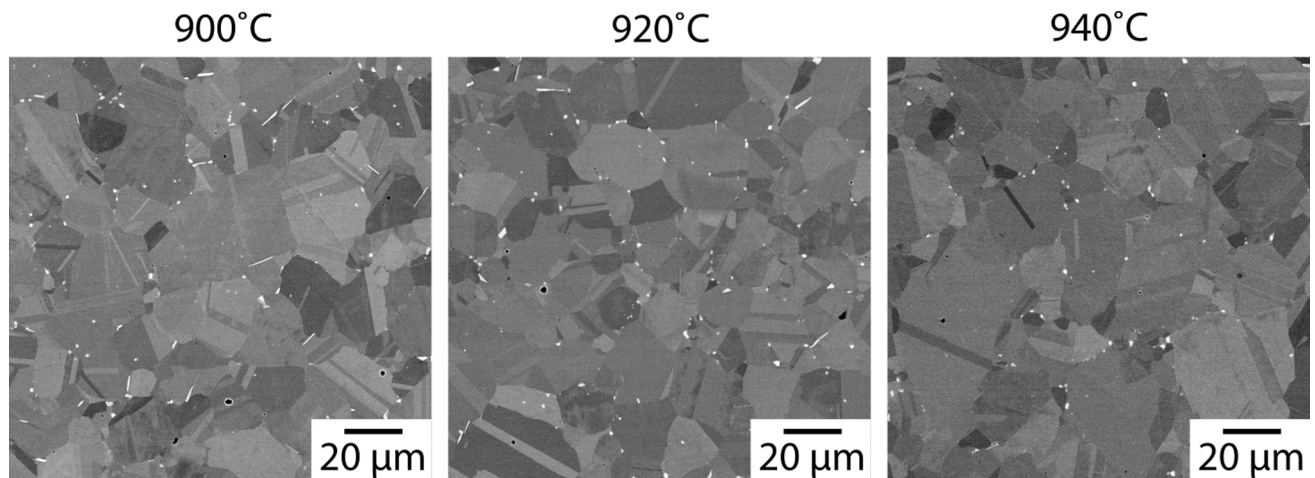

Fig. 8—SEM images of the alloy after exposure to 900 °C, 920 °C, and 940 °C for 100 hours.

this type, such as 718Plus.[30] In the As-HIP condition, the prior particle boundaries (PPBs) were decorated with MC and $M_{23}C_6$ carbides. After SHT, the boundaries were no longer continuously decorated, with isolated, bright contrast particles visible, suggesting coalescence of the phases previously decorating the PPBs. The SHT for 1 hour at 1030 °C followed by controlled cooling at 3 °C s^{-1} did not significantly affect the grain size, even though the heat treatment was above the γ' solvus. This is likely due to the Zener pinning effect of oxides, carbides, and oxy-carbides, as has been reported for the polycrystalline Ni-base superalloy RR1000.[60]

Predictions of the phase equilibria were obtained with the *Thermo-Calc* software, using the TTNi8 databases (version 8.2) and two different phase subsets.[61] Firstly, considering the γ and γ' phases alone, and secondly with the addition of the δ phase. Phase selection is important as the precipitation of the δ phase significantly alters the phase fractions of the γ and γ' due to the consumption of Nb. The results are presented in Table IV, where the effect of δ precipitation results in a significantly lower γ' fraction than predicted when excluding the δ phase. In this work, while the alloy does appear thermodynamically unstable with respect to δ phase formation, it was kinetically inhibited for exposure durations below
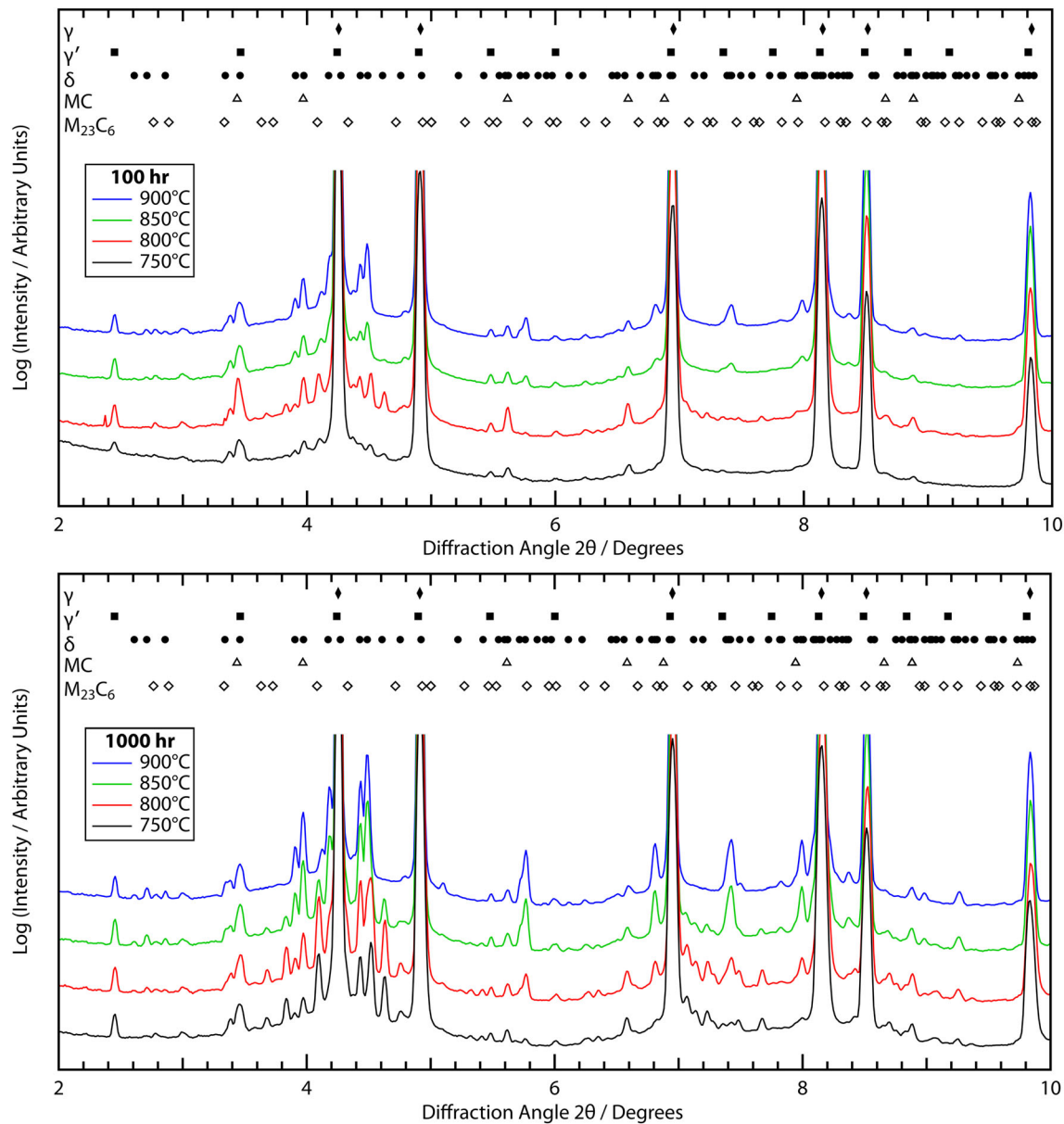
Fig. 9—sXRD patterns obtained from the alloy after SHT and subsequent aging at 750 °C, 800 °C, 850 °C, and 900 °C for 100 and 1000 hours.

100 hours. The δ phase was observed to form in the alloy after longer duration exposures, with a solvus temperature in the region of 940 °C based on the metallographic examination. Work on IN718 has shown evidence of δ precipitation after exposure durations of less than 10 hours at 750 °C, which suggests that the alloy studied in this work has a greater stability with respect to δ formation.[20]

The predicted solvus temperatures for the γ' and δ phases were obtained from *Thermo-Calc* as 960 °C for the γ' precipitates, and 999 °C for the δ phase. While there was reasonable agreement with the experimentally determined γ' solvus, the δ solvus was considerably higher than that observed, with similar offsets and discrepancies reported elsewhere.[62–64] The

microstructural examination performed indicates that the alloy does not form an initial population of δ phase after solution heat treatment, and the subsequent thermal exposures suggest that none would be expected after standard aging heat treatments. This contrasts with the alloy 718Plus, which contains a population of δ/η in billet material that can exhibit preferential orientations after deformation processing. This has been shown to result in both anisotropic fracture toughness and dwell crack growth behavior.[31,65,66] In the alloy studied here, with a δ solvus below that of the γ', careful optimization of the forging parameters will be required so that grain growth is controlled during supersolvus forging operations. This work forms part of a future study on this alloy.
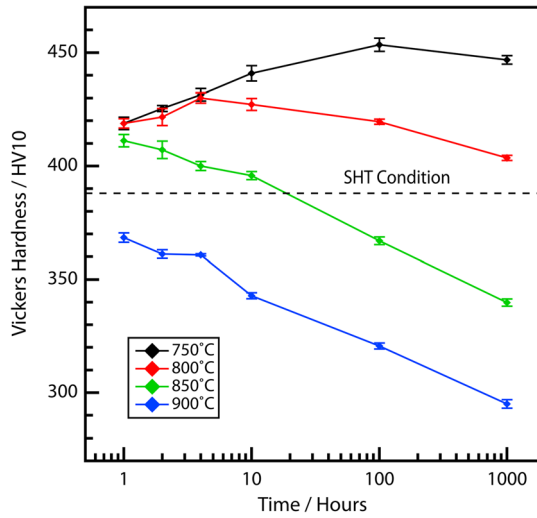
Fig. 10—Vickers hardness data (HV10) for the alloy after SHT and subsequent thermal exposures between 750 °C and 900 °C.

Table IV. Thermo-Calc Predicted Volume Fractions Considering the γ, γ', and δ Phases, or Only γ and γ' Phases

	750 °C	800 °C	850 °C	900 °C
γ	0.71	0.74	0.79	0.86
γ'	0.29	0.26	0.21	0.14
	750 °C	800 °C	850 °C	900 °C
γ	0.72	0.75	0.79	0.84
γ'	0.21	0.19	0.15	0.10
δ	0.07	0.07	0.06	0.06

B. Precipitate Evolution

The precipitate evolution after SHT was characterized by fitting the measured equivalent circular precipitate diameters after exposure for 4, 10, 100, and 1000 hours with the classic Lifshitz-Slyozov-Wagner (LSW) type model for diffusion-controlled precipitate coarsening (Eq. [1]).[67,68] These models seek to describe the temporal evolution of precipitate size, which tend to coarsen over time due to a thermodynamic driving force to lower the overall interfacial area. As a result of this driving force, larger precipitates tend to grow at the expense of smaller ones, in the process known as Ostwald ripening.[69]

LSW Coarsening Relationship (Eq. [1])

$$r_t^3 - r_0^3 = K_{\text{LSW}}t \qquad [1]$$

where r_t is the average precipitate radius at time t, r_0 is the starting precipitate size, and K_{LSW} is the coarsening rate constant. Due to the very fine starting precipitate size, r_0 is taken to be zero in this work.

The precipitate distributions in the samples with exposure durations up to 2 hours were too fine to be reliably characterized using the image analysis technique employed in this study. However, the cube of the measured precipitate radii obtained by log-normal fitting from the remaining samples is presented as a function of time in Figure 11(a), with the data for the samples exposed at 750 °C included in the inset graph for clarity. These data were fitted with a straight line to obtain an estimate of the coarsening rate constant, K_{LSW}, for each exposure temperature.

In the review by Baldan,[70] it was shown that the coarsening rate constants obtained at different temperatures, T, could be used to estimate the activation energy for precipitate coarsening. By assuming that the diffusion coefficient, D, can be described by an Arrhenius-type equation, then the coarsening rate constant can be expressed as shown in Eq. [2]:

Expression for the Coarsening Rate Constant (Eq. [2])

$$K_{\text{LSW}} = \frac{Ap_m^3}{RT}D_0\exp\left(\frac{-Q}{RT}\right) \qquad [2]$$

where A is a constant, p_m is the maximum precipitate size, R is the universal gas constant, D_0 is the diffusivity constant, and Q is the activation energy for coarsening.

By rearranging the expression and taking natural logs of both sides, Eq. [2] can be expressed as:

Rearrangement of the Expression for the Coarsening Rate Constant (Eq. [3])

$$\ln(K_{\text{LSW}}T) = \ln\left(\frac{Ap_m^3D_0}{R}\right) - \frac{Q}{RT} \qquad [3]$$

Therefore, plotting $\ln(K_{\text{LSW}}T)$ against $\frac{1}{T}$ should produce a straight line, with a gradient equal to $-\frac{Q}{R}$, from which the activation energy for diffusional coarsening could be calculated. A plot of this type is presented in Figure 11(b), where the estimated activation energy obtained of 333 ± 14 kJ mol^{-1} was consistent with literature values for similar Ni-base superalloys.[34,71,72]

Additionally, the graph in Figure 11(b) can also be used to estimate the coarsening rate constants at a chosen temperature by using the line of best fit to interpolate between the data points. A comparison of the rate constants obtained directly from fitting the precipitate radii data at a given temperature (Figure 11(a)) and those from the line of best fit considering all the exposure temperatures (Figure 11(b)) is presented in Table V. The values of the rate constants obtained from both methods are in good agreement with each other and are consistent with other reported values in the literature for the coarsening of the γ' precipitates in similar alloys such as IN718[73] and VDM780.[74]

The coarsening rate constants predicted by the model can be used to predict the expected precipitate diameter as a function of time at a given aging temperature. These are compared to the measured precipitate diameters in Figure 12. The precipitate diameters increase in size with exposure duration at a given aging temperature, as well as for increasing temperature at a given exposure duration. These were consistent with the qualitative observations made from the micrographs shown in
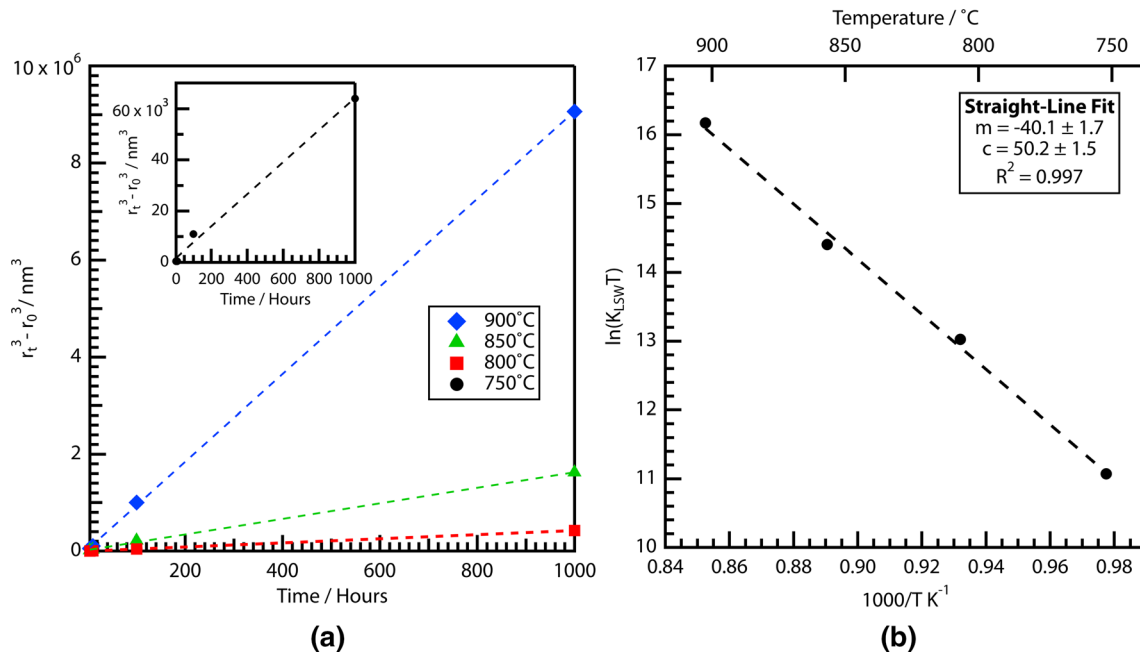
Fig. 11—(a) Plot of the cube of the measured precipitate radii as a function of time, with straight line fitting used to obtain the coarsening rate constants, K_{LSW}. (b) Arrhenius-type plot of K_{LSW} against $\frac{1}{T}$ used to model the rate constants as a function of temperature and calculate the activation energy for diffusion-controlled coarsening.

Table V. Comparison of Coarsening Rate Constants Obtained from the Measured Radii Data, and Those Predicted Using the Line of Best Fit Model

Temperature (°C)	K_{LSW}(Data) (nm^3 s^{-1})	K_{LSW}(Model) (nm^3 s^{-1})
750	0.0192	0.0178
800	0.0971	0.1051
850	0.4925	0.5290
900	2.4972	2.3162

Figure 6. After 1000 hours of thermal exposure, the precipitate diameters predicted by the model were 82, 141, 242, and 415 nm for aging temperatures 750 °C to 900 °C, respectively. These values and those obtained for the other aging temperatures and exposure durations match the experimentally measured values well. The quality of the fit suggests that the precipitate evolution observed is indeed governed by diffusion-controlled coarsening kinetics, as has been shown for several other polycrystalline Ni-base superalloys.[34,71,72,74,75]

To relate the observed hardening response to the precipitate coarsening, the APB$_{\{111\}}$ energy was calculated as a function of temperature using the Miodownik and Saunders method[76] and was found to vary from 189.0 mJ m^{-2} at 750 °C to 174.1 mJ m^{-2} at 900 °C. These are within the ranges commonly reported for other polycrystalline Ni alloys.[77] By using the calculated APB$_{\{111\}}$ energies alongside the Thermo-Calc predicted γ' volume fractions and γ' size estimated from the LSW modeling, the contributions to the critical resolved shear stress $\Delta\tau_{CRSS}$ from strong and weak-pair dislocation coupling were calculated. This followed the approach summarized by Kozar et al.[78] These were then plotted as a function of exposure time (a proxy for precipitate size) in Figure 13, where the expected dominant behavior (the mechanism with the lowest value of $\Delta\tau_{CRSS}$ for a given precipitate size) is highlighted with solid lines. The optimum precipitate size is typically defined at the transition from weak- to strong-pair dislocation coupling, and from these data were predicted as ≈ 38 nm, occurring after 105 hours at 750 °C and after 20 hours at 800 °C. These results correlate well with the actual hardening responses observed in the samples. The modeling does predict a modest hardening response after 3 hours at 850 °C, although this was not observed in practice. At 900 °C, strong-pair coupling is expected to be the dominant order hardening mechanism across the entire range of exposure durations studied, with no initial hardening predicted. While this analysis is insightful into potential routes for optimizing heat treatment schedules, it is noted that maximizing the strength of alloys in this way is not always advantageous. Controlled aging to give the precipitate size that results in the highest value of $\Delta\tau_{CRSS}$ may improve tensile strength, but monomodal precipitate distributions are likely to exhibit very poor ductility and limited creep performance.[79–81]

As grain size is known to provide a strengthening contribution via the Hall-Petch effect, the grain size was characterized in the sample exposed at 900 °C for 1000 hours.[82,83] The average grain size of 7 μm was not significantly different from the initial SHT condition
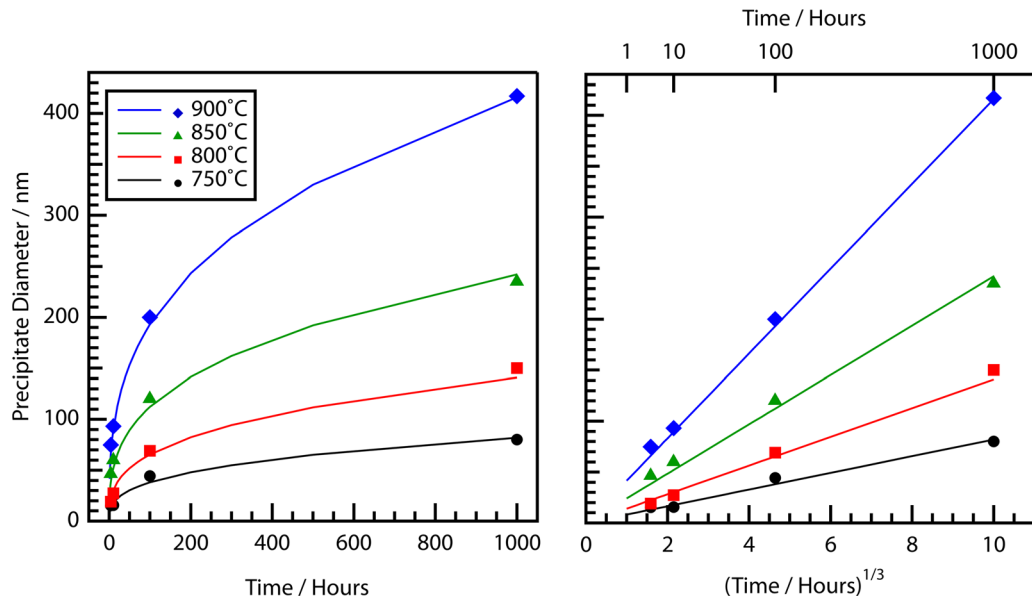
Fig. 12—Measured precipitate diameters (solid markers) plotted against time (left) and the cube root of time (right), with precipitate diameters calculated from the LSW model (solid lines).
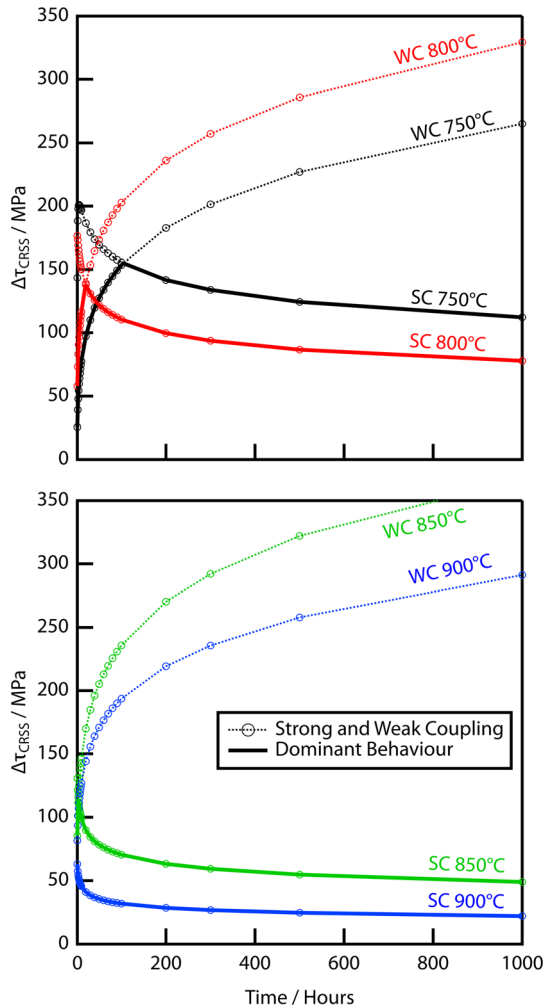

Fig. 13—Contributions to weak and strong-pair dislocation coupling for the different temperatures studied using the predicted γ' sizes from the LSW model and volume fractions from Thermo-Calc.

(see Electronic Supplementary Figure S1) to rationalize the observed changes in hardness and confirms these are most likely to be the result of the precipitate coarsening observed.

V. CONCLUSIONS

A new polycrystalline Ni-base superalloy has been characterized *via* scanning electron microscopy, synchrotron X-ray diffraction, and thermal analysis. The alloy was γ' forming, with evidence of δ phase formation after 100 hour exposure at 750 °C, offering improved thermal stability over IN718, which precipitates the δ phase after less than 10 hours at the same temperature.

The temporal evolution of the γ' precipitates was characterized, using a controlled cooling rate from SHT to ensure homogeneity of the initial microstructural condition. The results were rationalized through LSW modeling for diffusion-controlled precipitate coarsening and by comparing to estimates of strong- and weak-pair dislocation coupling. The predicted strengthening contributions correlated well to the observed hardening responses.

The combination of properties offered by this new alloy make it a promising candidate for further development of a low-cost Ni-base superalloy for structural applications at intermediate load and temperature service environments.

AUTHOR CONTRIBUTIONS

HJS contributed to conceptualization, HJS/GJW contributed to methodology, GJW contributed to formal analysis, GJW/NLC/CEPT/NGJ contributed to investigation, HJS/NGJ contributed to resources, GJW contributed to writing—original draft, HJS/GJW/NGJ contributed to writing—review and editing, GJW contributed to visualization, HJS/PMM/MCH contributed to supervision, HJS contributed to project administration, and HJS/MCH contributed to funding acquisition.

DATA AVAILABILITY

The research data required to reproduce these findings are available from the University of Cambridge repository[84]: https://doi.org/10.17863/CAM.94867.

CONFLICT OF INTEREST

OPEN ACCESS

SUPPLEMENTARY INFORMATION

The online version contains supplementary material available at https://doi.org/10.1007/s11661-023-07211-9.

REFERENCES

1. R.C. Reed: *The Superalloys: Fundamentals and Applications*, Cambridge University Press, Cambridge, 2006.
2. R. Darolia: *Int. Mater. Rev.*, 2019, vol. 64, pp. 355–80.
3. M.C. Hardy, B. Zirbel, G. Shen, and R. Shankar: *Proceedings of the International Symposium on Superalloys*, 2004, pp. 83–90.
4. T.P. Gabb, J. Telesman, P.T. Kantzos, and K. O'Connor: NASA Technical Report, 2002, pp. 1–51.
5. S.T. Wlodek, M. Kelly, and D.A. Alden: in *Superalloys 1996 (Eighth International Symposium)*, R.D. Kissinger, D.J. Deye, D.L. Anton, A.D. Cetel, M.V. Nathal, T.M. Pollock, D.A. Woodford, eds., TMS, 1996, pp. 129–36.
6. D.D. Krueger, R.D. Kissinger, and R.G. Menzies: in *Superalloys 1992*. D. Anton, T. Khan, R. Kissinger, and D. Klarstrom, eds., The Minerals, Metals & Materials Society, 1992, pp. 277–86.
7. A.F. Giamei and B.H. Kear: *Metall. Trans.*, 1970, vol. 1, pp. 2185–92.
8. P.D. Genereux and C.A. Borg: in: Supperalloys 2000 (Ninth International Symposium). *TMS*, 2000, vol. 2000, pp. 19–27.
9. S.T. Wlodek and R.D. Field: in *Superalloys 718, 625, 706 and Various Derivatives (1994)*, TMS, 1994, pp. 167–76.
10. P. Auburtin, S.L. Cockcroft, A. Mitchell, and A.J. Schmalz: in *Superalloys 718, 625, 706 and Various Derivatives (1997)*, TMS, 1997, pp. 47–54.
11. L.A. Jackman, G.E. Maurer, and S. Widge, in *Superalloys 718, 625, 706 and Various Derivatives (1994)*, TMS, 1994, pp. 153–66.
12. R.M.F. Jones and L.A. Jackman: *JOM*, 1999, vol. 51, pp. 27–31.
13. R. Couturier, H. Burlet, S. Terzi, S. Dubiez, G. Raisson, and L. Guetaz: in *Supperalloys 2004 (Tenth International Symposium)*, TMS, 2004, pp. 351–59.
14. M. Fahrmann and A. Suzuki: in *Supperalloys 2008 (Eleventh International Symposium)*, TMS, 2008, pp. 311–16.
15. C.A. Dandre, C.A. Walsh, R.W. Evans, R.C. Reed, and S.M. Roberts: in *Supperalloys 2000 (Ninth International Symposium)*, TMS, 2000, pp. 85–94.
16. M.C. Hardy, M. Detrois, E.T. McDevitt, C. Argyrakis, V. Saraf, P.D. Jablonski, J.A. Hawk, R.C. Buckingham, H.S. Kitaguchi, and S. Tin: *Metall. Mater. Trans. A*, 2020, vol. 51A, pp. 2626–50.
17. D.F. Paulonis, J.M. Oblak, and D.S. Duvall: *Trans. ASM*, 1969, vol. 62, pp. 611–22.
18. J.M. Oblak, D.F. Paulonis, and D.S. Duvall: *Metall. Trans.*, 1974, vol. 5, pp. 143–53.
19. J.M. Oblak, D.S. Duvall, and D.F. Paulonis: *Mater. Sci. Eng.*, 1974, vol. 13, pp. 51–56.
20. A. Oradei-Basile and J.F. Radavich: in *Superalloys 718, 625 and Various Derivatives (1991)*, TMS, 1991, pp. 325–35.
21. A. Lingenfelter: in *Superalloys 718 Metallurgy and Applications (1989)*, TMS, 1989, pp. 673–83.
22. J.M. Moyer, L.A. Jackman, C.B. Adasczik, R.M. Davis, and R. Forbes-Jones: in *Superalloys 718, 625, 706 and Various Derivatives (1994)*, TMS, 1994, pp. 39–48.
23. J.J. Debarbadillo and S.K. Mannan: *JOM*, 2012, vol. 64, pp. 265–70.
24. R.P. Badrak: in *8th International Symposium on Superalloy 718 and Derivatives 2014*, 2014, pp. 493–502.
25. G. Wiese, H. John, X. Liu, and J. Xu: in *7th International Symposium on Superalloy 718 and Derivatives (2010)*, Wiley, Hoboken, 2010, pp. 923–32.
26. R.B. Bhavsar, A. Collins, and S. Silverman: *Proc. Int. Symp. Superalloys Various Deriv.*, 2001, vol. 1, pp. 47–55.
27. T.A. Phillips and A.S.M. Handbook: *ASM Handbook Properties & Selection: Irons Steels and High-Performace Alloys*, 1990, vol. 1, pp. 1023–33.
28. A. Verma, B. Paul, J. Singh, K. Ramaswamy, S. Nalawade, and S. Mahadevan: in *7th International Symposium on Superalloy 718 and Derivatives (2010)*, Wiley, Hoboken, 2010, pp. 737–50.
29. Y. Desvallees, M. Bouzidi, F. Bois, and N. Beaude: in *Superalloys 718, 625, 706 and Various Derivatives (1994)*, TMS, 1994, pp. 281–91.
30. R.L. Kennedy: in *Superalloys 718, 625, 706 and Derivatives 2005*. E.A. Loria, ed., The Minerals, Metals & Materials Society, 2005, pp. 1–4.

31. D. Huenert, M. Proebstle, A. Casanova, R. Schluetter, R. Krakow, M. Buescher, P. Randelzhofer, A. Evans, K. Loehnert, T. Witulski, S. Neumeier, and C. Rae: in *Proceedings of the International Symposium on Superalloys*, 2016.

32. P.W. Keefe, S.O. Mancuso, and G.E. Maurer: in *Superalloys 1992 (Seventh International Symposium)*, TMS, 1992, pp. 487–96.

33. J.A. Heaney, M.L. Lasonde, A.M. Powell, B.J. Bond, and C.M. O'Brien: in *8th International Symposium on Superalloy 718 and Derivatives*, Wiley, Hoboken, 2014, pp. 67–77.

34. T. Billot, J. Cormier, J. Franchet, A. Laurence, P. Villechaise, and A. Wessman: in *Proceedings of the 13th International Symposium on Superalloys*, The Minerals, Metals & Materials Society, 2016, pp. 793–800.

35. M. Pérez, C. Dumont, and S. Nouveau: *Miner. Metals Mater. Ser.*, 202, pp. 441–49.

36. W. Buchmann, S. Charmond, C. Crozet, A. Devaux, R. Forestier, D. Helm, and M. Hueller: in *Proceedings of the 13th International Symposium on Superalloys*, The Minerals, Metals & Materials Society, 2016, pp. 437–46.

37. M.A. Charpagne, J.M. Franchet, and N. Bozzolo: *Mater. Des.*, 2018, vol. 144, pp. 353–60.

38. M.A. Charpagne, T. Billot, J.M. Franchet, and N. Bozzolo: *J. Alloys Compd.*, 2016, vol. 688, pp. 685–94.

39. C. O'Brien, J. Heaney, J. Russell, M. Lasonde, and B. Bond: in *8th International Symposium on Superalloy 718 and Derivatives (2014)*, Wiley, Hoboken, 2014, pp. 107–18.

40. A. Devaux, B. Picque, M. Gervais, E. Georges, T. Poulain, and P. Heritier: in *Superalloys 2012 (Twelfth International Symposium)*, Wiley, Hoboken, 2012, pp. 911–19.

41. A. Devaux, E. Georges, and P. Héritier: *7th International Symposium on Superalloy 718 and Derivatives 2010*, 2010, pp. 223–35.

42. M. Pérez, C. Dumont, O. Nodin, and S. Nouveau: *Mater Charact*, 2018, vol. 146, pp. 169–81.

43. T. Konkova, S. Rahimi, S. Mironov, and T.N. Baker: *Mater Charact*, 2018, vol. 139, pp. 437–45.

44. A. Coyne-Grell, J. Blaizot, S. Rahimi, I. Violatos, S. Nouveau, C. Dumont, A. Nicolaÿ, and N. Bozzolo: *J. Alloys Compd.*, 2022, vol. 916, 165465.

45. T. Fedorova, J. Rösler, J. Klöwer, and B. Gehrmann: in *8th International Symposium on Superalloy 718 and Derivatives*, 2014, pp. 587–99.

46. J. Sharma, M.H. Haghighat, B. Gehrmann, C. Moussa, and N. Bozzolo, in *Superalloys 2020*, 2020, pp. 450–60.

47. M.C. Hardy, H.J. Stone, N.G. Jones, and P. Mignanelli: United States Patent US010287654B2 Ni-Base Alloy For Structural Applications, US Patent: A Nickel Base Alloy for Structural Applications US10287654B2, 2019.

48. M.C. Hardy, M. Hafez Haghighat, C. Argyrakis, R.C. Buckingham, A. La Monaca, and B. Gehrmann: *Miner. Metals Mater. Ser.*, 2023, pp. 29–47.

49. M. Drakopoulos, T. Connolley, C. Reinhard, R. Atwood, O. Magdysyuk, N. Vo, M. Hart, L. Connor, B. Humphreys, G. Howell, S. Davies, T. Hill, G. Wilkin, U. Pedersen, A. Foster, N. De Maio, M. Basham, F. Yuan, and K. Wanelik: Urn:Issn:1600-5775 22, 2015, pp. 828–38.

50. D.Š Jung, T. Donath, O. Magdysyuk, and J. Bednarcik: *Powder Diffr.*, 2017, vol. 32, pp. S22-27.

51. M.L. Hart, M. Drakopoulos, C. Reinhard, T. Connolley, Urn:Issn:0021-8898 46 (2013) 1249–60.

52. J. Filik, A.W. Ashton, P.C.Y. Chang, P.A. Chater, S.J. Day, M. Drakopoulos, M.W. Gerring, M.L. Hart, O. V. Magdysyuk, S. Michalik, A. Smith, C.C. Tang, N.J. Terrill, M.T. Wharmby, and H. Wilhelm: Urn:Issn:1600-5767 50, 2017, pp. 959–66.

53. M. Basham, J. Filik, M.T. Wharmby, P.C.Y. Chang, B. El Kassaby, M. Gerring, J. Aishima, K. Levik, B.C.A. Pulford, I. Sikharulidze, D. Sneddon, M. Webber, S.S. Dhesi, F. Maccherozzi, O. Svensson, S. Brockhauser, G. Náray, and A.W. Ashton: *J. Synchrotron Radiat.*, 2015, vol. 22, pp. 853–58.

54. M. Preuss, P.J. Withers, J.W.L. Pang, and G.J. Baxter: *Metall. Mater. Trans. A*, 2002, vol. 33A, pp. 3215–25.

55. D. Freedman and P. Diaconis: *Zeitschrift Für Wahrscheinlichkeitstheorie Und Verwandte Gebiete*, 1981, vol. 57, pp. 453–76.

56. D.L. Sponseller: in *Superalloys 1996 (Eighth International Symposium)*, TMS, 1996, pp. 259–70.

57. A. Mitchell: in *7th International Symposium on Superalloy 718 and Derivatives 2010*, 2010, pp. 161–67.

58. K.A. Christofidou, M.C. Hardy, H.Y. Li, C. Argyrakis, H. Kitaguchi, N.G. Jones, P.M. Mignanelli, A.S. Wilson, O.M.D.M. Messé, E.J. Pickering, R.J. Gilbert, C.M.F. Rae, S. Yu, A. Evans, D. Child, P. Bowen, and H.J. Stone: *Metall. Mater. Trans. A*, 2018, vol. 49A, pp. 3896–3907.

59. A. Aghajani, J. Tewes, A.B. Parsa, T. Hoffmann, A. Kostka, and J. Kloewer: *Metall. Mater. Trans. A*, 2016, vol. 47A, pp. 4382–92.

60. D.M. Collins, B.D. Conduit, H.J. Stone, M.C. Hardy, G.J. Conduit, and R.J. Mitchell: *Acta Mater.*, 2013, vol. 61, pp. 3378–91.

61. J.O. Andersson, T. Helander, L. Höglund, P. Shi, and B. Sundman: *Calphad*, 2002, vol. 26(2), pp. 273–312.

62. A.S. Wilson, M.C. Hardy, and H.J. Stone: *J. Alloys Compd.*, 2019, vol. 789, pp. 1046–55.

63. O.M. Horst, D. Schmitz, J. Schreuer, P. Git, H. Wang, C. Körner, and G. Eggeler: *J. Mater. Sci.*, 2021, vol. 56, pp. 7637–58.

64. R.B. Frank, C.G. Roberts, J. Zhang, 7th International Symposium on Superalloy 718 and Derivatives 2010 2 (2010) 725–36.

65. C. Kienl, P. Mandal, H. Lalvani, and C.M.F. Rae: *Metall. Mater. Trans. A*, 2020, vol. 51A, pp. 4008–21.

66. A. Casanova, M. Hardy, D. Huenert, K. Loehnert, and C. Rae: in *Proceedings of the 13th International Symposium on Superalloys*, M. Hardy, E. Huron, U. Glatzel, B. Griffin, B. Lewis, C. Rae, V. Seetharaman, and S. Tin, eds., The Minerals, Metals & Materials Society, Hoboken, 2016, pp. 427–436.

67. I.M. Lifshitz and V.V. Slyozov: *J. Phys. Chem. Solids*, 1961, vol. 19, pp. 35–50.

68. C. Wagner: *Zeitschrift Für Elektrochemie, Berichte Der Bunsengesellschaft Für Physikalische Chemie*, 1961, vol. 65, pp. 581–91.

69. H.A. Calderon, P.W. Voorhees, J.L. Murray, and G. Kostorz: *Acta Metall. Mater.*, 1994, vol. 42, pp. 991–1000.

70. A. Baldan: *J. Mater. Sci.*, 2002, vol. 37, pp. 2171–2202.

71. F. Masoumi, M. Jahazi, D. Shahriari, and J. Cormier: *J. Alloys Compd.*, 2016, vol. 658, pp. 981–95.

72. B. Flageolet, P. Villechaise, M. Jouiad, and J. Mendez: in *Superalloys 2004 (Tenth International Symposium)*, TMS, 2004, pp. 371–79.

73. Y. Han, P. Deb, and M.C. Chaturvedi: *Metal Sci.*, 1982, vol. 16, pp. 555–62.

74. C. Solís, A. Kirchmayer, I. da Silva, F. Kümmel, S. Mühlbauer, P. Beran, B. Gehrmann, M.H. Haghighat, S. Neumeier, and R. Gilles: *J. Alloys Compd.*, 2022, vol. 928, 167203.

75. G.A. Zickler, R. Radis, R. Schnitzer, E. Kozeschnik, M. Stockinger, and H. Leitner: *Adv. Eng. Mater.*, 2010, vol. 12, pp. 176–83.

76. A.P. Miodownik and N. Saunders: in *Applications of Thermodynamics to the Synthesis and Processing of Materials*, The Minerals, Metals & Materials Society, 1995.

77. D.J. Crudden, A. Mottura, N. Warnken, B. Raeisinia, and R.C. Reed: *Acta Mater.*, 2014, vol. 75, pp. 356–70.

78. R.W. Kozar, A. Suzuki, W.W. Milligan, J.J. Schirra, M.F. Savage, and T.M. Pollock: *Metall. Mater. Trans. A*, 2009, vol. 40A, pp. 1588–603.

79. D.M. Collins and H.J. Stone: *Int. J. Plast.*, 2014, vol. 54, pp. 96–112.

80. D. Locq, P. Caron, S. Raujol, F. Pettinari-Sturmel, A. Coujou, and N. Clement: in *Superalloys 2004 (Tenth International Symposium)*, TMS, 2004, pp. 179–87.

81. R.A. Stevens and P.E.J. Flewitt: *Mater. Sci. Eng.*, 1979, vol. 37, pp. 237–47.

82. N.J. Petch: *Journal of the Iron and Steel Institute*, 1953, vol. 174, pp. 25–28.

83. E.O. Hall: *Proc. Phys. Soc. Sect. B*, 1951, vol. 64, pp. 747–53.

84. G. Wise, N. Church, C. Talbot, P. Mignanelli, M. Hardy, N. Jones, and H. Stone: Research Data Supporting, Microstructural Stability and Evolution in a New Polycrystalline Ni-Base Superalloy, 2023.